

A Numerical Study on Faraday-Type Electromagnetic Flowmeter in Liquid Metal System, (I)

A Numerical Method Based on Magnetic Field and Electric Potential Field: FALCON Code

Takeshi SHIMIZU^{*1,†}, Noriyuki TAKESHIMA^{*2} and Noboru JIMBO^{*2}

^{*1}*Nuclear Engineering Laboratory, Toshiba Corporation*

^{*2}*Isogo Nuclear Engineering Center, Toshiba Corporation*

(Received September 16, 1999), (Revised January 14, 2000)

To predict the three-dimensional steady-state structure of electromagnetic phenomena in the Faraday-type Electromagnetic Flowmeter (EMF), a numerical simulation method using the Galerkin finite element method has been adopted and formatted as a computer code, FALCON.

As the induction equation for the induced magnetic field that is important in a liquid metal system, we have presented $\mathbf{B}-\phi$ formulation for the induced magnetic field and the electric potential field and $\mathbf{A}-\phi$ formulation for the vector potential field and the electric potential field, and compared the computational efficiency of both formulations. We have selected the $\mathbf{B}-\phi$ formulation. The computer simulation of the EMF of the MONJU secondary cooling system has been performed and the calculations have shown a good agreement with the calibration test data. We have investigated qualitatively how far the influence of the end effect extends and the characteristics of the voltage response.

Overall, this study has indicated that the present method can be applied to the estimation of the characteristics of an EMF and the design of a new EMF.

KEYWORDS: *electromagnetic flowmeter, liquid metals, end effects, induced current, induced magnetic fields, fully developed turbulent flow, LMFBR type reactors, finite element method, Galerkin method, computer programs, FALCON, numerical solution*

I. Introduction

Sodium coolant flow measurements in Liquid Metal Fast Breeder Reactor (LMFBR) main cooling systems, that is, the primary and secondary circuits, must be made not only to monitor the reactor plant operation, but also to lead the plant protection system operation. In liquid metal systems, the Venturi flowmeter and Faraday-type Electromagnetic Flowmeter (EMF) are often used. In LMFBR main cooling systems, the EMF is particularly suitable for control system and plant protection system use, because the EMF has more rapid response time and simpler structure than the Venturi flowmeter, and no parts assembled through the pipe wall.

The EMF, a simple device composed of a magnetic apparatus and electrodes is applied extensively in water systems in various parts of the world. However, a phenomenon different from that in a water system appears in a liquid metal system, *i.e.* an induced electric current flows in a conducting fluid by an electromotive force which the fluid motion in a magnetic field generates. The

characteristics of the EMF are dependent on the electromotive force which is determined by the distribution of magnetic fields applied by the magnetic apparatus and induced by the electric current and the distribution of the conducting fluid flow. The distribution of the induced magnetic field becomes complex because of the three-dimensional feature of the electric current and the diffusion and convection mechanism of the magnetic field itself. It is costly and time consuming to study such a three-dimensional complex electromagnetic phenomenon by experiments. To avoid the high cost and the necessity of a long series of experiments, there is a need for a numerical simulation technique based on refined electromagnetic modeling that is capable of providing sufficient information for understanding the phenomena theoretically and designing an EMF.

The objectives of the present study are to develop a new numerical simulation code for calculating fine structure of the three-dimensional steady-state induced magnetic field and electric potential field in the EMF, discuss the accuracy of the numerical method by comparing calculated results with measured data, and clarify the effect of the induced magnetic field on the EMF characteristics.

Many theoretical and numerical studies on EMFs have been performed. Use of a weight function for the estimation of output voltage in a water system was first

^{*1} *Ukishima-cho, Kawasaki-ku, Kawasaki 210-0862.*

^{*2} *Sinsugita-cho, Isogo-ku, Yokohama 235-8523.*

[†] Corresponding author, Tel. +81-44-288-8142, Fax. +81-44-270-1806, E-mail: takeshi3.shimizu@toshiba.co.jp

proposed by Shercliff⁽¹⁾, and in an extension of this idea, Bevir proposed the use of a weight vector⁽²⁾. Using a weight function, Kuromori⁽³⁾ studied EMFs with plural pairs of electrodes. Because the electric conductivity of water is very small compared to that of liquid metal fluid, the induced magnetic field generated by the induced current flow in water is negligible with respect to the applied magnetic field. These ideas of the weight function and the weight vector are useful for analyzing the characteristics of EMFs in a water system. However, the electric conductivity of liquid metal fluid is very large compared with that and therefore the induced magnetic field cannot be disregarded. Namely, the weight function is not applicable in a liquid metal system because it depends on a flow velocity distribution. Moreover, electromagnetic phenomena in an EMF become more complex; for example, the output voltage of an EMF is not strictly proportional to the flow due to the end effect and is influenced by the three-dimensional profile of a flow velocity field. Another approach is needed for the estimation of these complex phenomena. Kobayashi *et al.*⁽⁴⁾ studied analytically the end effect of an EMF in a liquid metal system. Shimizu *et al.*⁽⁵⁾ studied the effect of swirling flow profiles on the output voltage of EMFs with a two-dimensional electromagnetic analysis method. In these studies, instead of the former approach based on the weight function, new approaches were used in which a governing equation of the induced magnetic field was solved directly. However these analysis methods are insufficient for treating arbitrary three-dimensional profiles of an applied magnetic field and a flow velocity field. This is the motivation for the present study on a numerical technique available under more realistic conditions. We develop a three-dimensional steady-state electromagnetic analysis code, FALCON (a Finite element Analysis code for Liquid metal fluid with highly electric CONducting property). The FALCON code adopts the Galerkin finite element method using isoparametric elements and a procedure of finite element generation using a curvilinear coordinate system.

In this paper we present and discuss two numerical formulations based on two induction equations for an induced magnetic field and for a vector potential. We format both the formulations as a computer code, FALCON, and compare the computing efficiency of both the formulations. With the FALCON code we simulate the calibration test⁽⁶⁾ for the EMF in the A-loop of the secondary cooling system of the Japanese Prototype Fast Breeder Reactor, "MONJU", and compare the results with the calibration test data. Finally, we analyze the numerical and experimental results through the dimensionless electromagnetic expression and discuss the effect of the induced magnetic field on the characteristics of the EMF.

II. Governing Equations

Figure 1 shows a schematic of the standard Faraday-

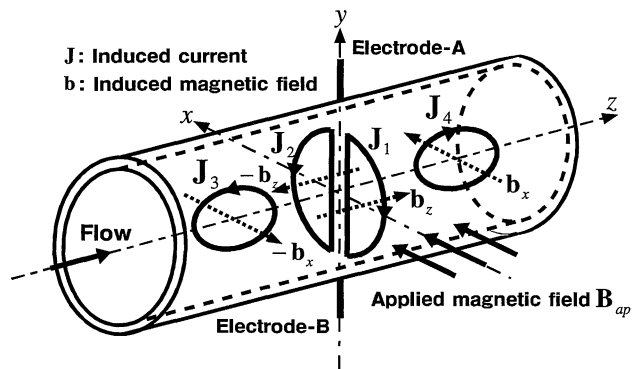


Fig. 1 Typical induced currents and magnetic fields in Faraday-type electromagnetic flowmeter

type electromagnetic flowmeter in a liquid metal system. It is constructed from a pair of electrodes (denoted Electrode A and Electrode B in the figure) welded to a pipe, and a magnetic apparatus by which an applied magnetic field is produced. In the liquid metal system, permanent magnets are usually used as the magnetic apparatus. The flow of liquid metal fluid in the pipe can be determined by measuring the electric potential difference between a pair of the electrodes.

Before deriving steady-state governing equations, we adopt the following assumptions in the EMF to be analyzed:

- (1) the coolant flow is not affected by an electromagnetic force and also the applied magnetic field is not affected by electromagnetic phenomena in the EMF,
- (2) the volume density of electric charge is negligible because the liquid metal fluid and pipe have a highly electric conducting property, and therefore displacement currents induced by electric polarization can be neglected with respect to induced currents,
- (3) the liquid metal fluid and pipe have a non-magnetized property, and the magnetic permeability and the electric conductivity are isotropic, and
- (4) the liquid metal fluid is incompressible.

Based on Maxwell's equation, Ohm's law in the laboratory system and above assumptions, the following steady-state induction equation and electric potential equation are obtained in moving fluids:

$$\nabla \times \left(\frac{\mathbf{b}}{\mu_0} \right) = \sigma[\mathbf{E} + \mathbf{u} \times (\mathbf{B}_{ap} + \mathbf{b})], \quad (1)$$

$$\nabla(\sigma \nabla \phi) = \nabla[\sigma \mathbf{u} \times (\mathbf{B}_{ap} + \mathbf{b})], \quad (2)$$

where \mathbf{b} is the induced magnetic field, σ is the electric conductivity and μ_0 is the magnetic permeability of vacuum. We have treated the applied magnetic field \mathbf{B}_{ap} and the flow velocity distribution \mathbf{u} as information input for the solution of these governing equations. The governing equations in the pipe are obtained after neglecting the velocity field in Eqs. (1) and (2). On the inner boundary surface between the liquid metal and the pipe, the condition that the magnetic field is continuous is imposed.

Here we discuss whether the solution \mathbf{b} of Eq. (1) is uniquely defined. If Eq. (1) is satisfied by two different solutions \mathbf{b} and \mathbf{b}' , the divergence of the residual that remains after one equation is subtracted from another is described, as follows:

$$\nabla \left[\nabla \times \left(\frac{\mathbf{d}}{\mu_o} \right) \right] - \sigma \nabla (\mathbf{u} \times \mathbf{d}) = 0, \quad (3)$$

where $\mathbf{d} = \mathbf{b} - \mathbf{b}'$. The first term of Eq. (3) is always equal to zero for an arbitrary vector \mathbf{d} , and therefore, if \mathbf{u} is not equal to zero, \mathbf{d} must be equal to zero. Namely, Eq. (1) has a unique solution only when \mathbf{u} is not equal to zero. Under the condition that \mathbf{u} is zero, the solution seems not to be unique but it can be uniquely defined by imposing the following conservation equation:

$$\nabla \mathbf{b} = 0. \quad (4)$$

As a result, the induced magnetic field and the electric potential field in the EMF can be determined from the governing Eqs. (1), (2) and (4).

We can introduce two formulations to solve the governing equations. One is based on the induced magnetic field and the electric potential field (\mathbf{B} - ϕ formulation). Another is based on the vector potential field and the electric potential field (\mathbf{A} - ϕ formulation). These two formulations are described below in the Cartesian coordinate system.

1. \mathbf{B} - ϕ Formulation

After rearranging the curl of Eq. (1) and applying the mathematical formulas (A1) and (A2) described in APPENDIX 1 and then eliminating several terms by using conservation equations of magnetic field and flow velocity field, the following steady-state governing equation of the induced magnetic field in the liquid metal fluid and the pipe is obtained, as follows:

$$\begin{aligned} -\nabla^2 \left(\frac{\mathbf{b}}{\mu_o} \right) - \sigma [(\mathbf{b} \nabla) \mathbf{u} - (\mathbf{u} \nabla) \mathbf{b}] \\ = \sigma [(\mathbf{B}_{ap} \nabla) \mathbf{u} - (\mathbf{u} \nabla) \mathbf{B}_{ap}]. \end{aligned} \quad (5)$$

After disregarding the velocity variable, Eqs. (2) and (5) can be also used as the governing equations in the pipe.

2. \mathbf{A} - ϕ Formulation

As the induced magnetic field \mathbf{b} satisfies the conservation relation (4), it is represented mathematically by a vector potential \mathbf{A} , as follows:

$$\nabla \times \mathbf{A} = \mathbf{b}. \quad (6)$$

Equations (1) and (6) lead to the following induction equation by applying the Coulomb gauge and the mathematical formula (A1):

$$-\nabla \left(\frac{1}{\mu_o} \nabla \mathbf{A} \right) + \sigma \nabla \phi - \sigma \mathbf{u} \times (\nabla \times \mathbf{A}) = \sigma \mathbf{u} \times \mathbf{B}_{ap}. \quad (7)$$

Equations (2) and (6) lead to the electric potential equation, as follows:

$$\nabla (\sigma \nabla \phi) = \nabla [\sigma \mathbf{u} \times (\nabla \times \mathbf{A}) + \alpha \mathbf{u} \times \mathbf{B}_{ap}]. \quad (8)$$

The governing equations (7) and (8) can be also applied in the pipe after disregarding the velocity variable.

III. Numerical Procedure

We have used the Galerkin finite element method (GFEM)⁽⁷⁾⁽⁸⁾ with biquadratic Serendipity isoparametric finite elements (based on a 27 nodes-cubic element) to generate a set of discrete equations from the governing equations, because the curved geometry of the pipe and the electromagnetic boundary condition can be treated accurately. Procedures of finite element generation and discretization of the governing equations are described in this chapter.

1. Finite Element Generation Technique

Firstly, analysis domain of the EMF is divided in the axial direction, *i.e.* in the direction of the coordinate z . Secondly, to construct lattice on each cross section of the pipe, we have adopted the curvilinear coordinate system which is determined by the Laplacian or Poisson equation⁽⁹⁾. The equation of the transformation relation is solved by using the point SOR method with the Dirichlet boundary condition applied on the outer boundary of the cross section. In this method, a suitable choice of the transformed space is important for obtaining desired coordinate lines in the physical space. We adopted a procedure of multi-connected transformed space⁽¹⁰⁾, *i.e.* a physical domain to be analyzed is decomposed into several local regions, and then each local region is projected on suitable transformed space. Figure 2 shows a sample grid scheme for analysis domain of the EMF exhibited in Fig. 1. In this case, the domain of the liquid metal fluid is decomposed into an inner region and an immediate

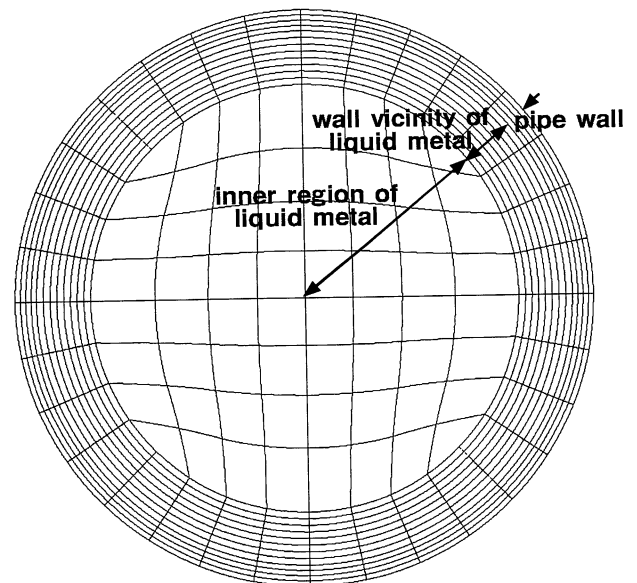


Fig. 2 A mesh scheme on cross section of analysis domain

vicinity of the pipe wall. A grid scheme in the inner region is constructed by the curvilinear coordinate lines. In the immediate vicinity of the pipe wall, a gradient of the turbulent flow velocity in the radial direction is steep and the induced current density is large. To solve the governing equations accurately under such a condition, care is taken in this local region such that lattice lines are made parallel and orthogonal to the pipe wall. By using such a lattice arrangement, the lattice interval can be controlled easily to keep accuracy of predictions. On the cross-section at all the axial grid points, the same mesh scheme shown in Fig. 2 is adopted. We apply finer axial division in the domain surrounded by the magnetic apparatus and in its downstream region where the induced magnetic field is transported by the liquid metal fluid flow. Three-dimensional finite elements are constructed based on these grid lines.

2. Discretization by Finite Element Method

We describe discretizations of the governing equations by the GFEM in the Cartesian coordinate system. The start point of the GFEM is to assume the following approximate solution Y in each element, *i.e.* the induced magnetic flux density b_i , the vector potential A_i or the electric potential ϕ . We adopt biquadratic Serendipity isoparametric elements (27 nodes-cubic), because circular geometry of a pipe can be treated exactly:

$$Y = \sum_{l=1}^{27} \varphi_l(\xi_\lambda) Y_l, \quad (9)$$

where φ is a biquadratic shape function, Y_l is each solution at the λ -th node and ξ_λ ($\lambda = 1, 3$) is the normalized curvilinear coordinate in the finite elements.

(1) Discretization of \mathbf{B} - ϕ Formulation

Firstly, we describe the discretization of the induction equation (5). After integrating the weighted residual of the induction equation (5) over a finite element volume V and then applying the weak formulation into the diffusion term of the induced magnetic flux density, the equation of a finite element is obtained as the i -component in the Cartesian coordinate system, as follows:

$$\begin{aligned} & \frac{1}{\mu_o} \int_V \nabla \omega \nabla b_i dV - \sigma \int_V \omega [(\mathbf{b} \nabla) \mathbf{u} + (\mathbf{u} \nabla) \mathbf{b}]_i dV \\ & = \sigma \int_V \omega [(\mathbf{B}_{ap} \nabla) \mathbf{u} + (\mathbf{u} \nabla) \mathbf{B}_{ap}]_i dV \\ & + \frac{1}{\mu_o} \int_S \omega (\nabla b_i) \mathbf{n} dS, \end{aligned} \quad (10)$$

where ω is the weighting function, S denotes the surface of the element, and \mathbf{n} is the outward normal vector on the surface of the element. The second integral of the left-hand side of Eq. (10) represents transport of the induced magnetic field by the liquid metal flow. To keep the stability of the solution in large Reynolds number condition, we employ an upwind scheme, *i.e.* the Petrov Galerkin method⁽¹¹⁾, only in the axial direction. Also, in the pipe wall region where $\mathbf{u} = 0$, the shape function

of Eq. (9) is used as the weighting functions ω , *i.e.* the Bubnov Galerkin method⁽⁸⁾ is used.

In a way similar to the above formulation, an integral equation of weighted residuals of the electric potential equation (2) in the finite element V can be described as follows:

$$\begin{aligned} \int_V \nabla \omega \sigma \nabla \phi dV & = \int_V \nabla \omega \sigma \mathbf{u} \times (\mathbf{b} + \mathbf{B}_{ap}) dV \\ & + \int_S \omega \sigma \nabla \phi \mathbf{n} dS \\ & - \int_S \omega \sigma \mathbf{u} \times (\mathbf{b} + \mathbf{B}_{ap}) \mathbf{n} dS, \end{aligned} \quad (11)$$

where the weak formulation is applied to the diffusion term and the electromotive force term, and the shape function of Eq. (9) is used as the weighting functions ω .

Element-wise discrete equations of the induction equation (5) can be obtained by substituting approximate solution (9) into Eq. (10). After assembling all the element-wise discrete equations in the whole analysis domain specified, a global system of simultaneous equations is obtained. In the same way, a global simultaneous equation system of the electric potential equation (2) is obtained from Eq. (11).

To completely determine the solutions, we discuss boundary conditions that are imposed upon the two global systems of simultaneous equations. The surface integral terms of Eq. (10) on the boundary surface of adjacent elements cancel each other and remain only on the outer boundary surface. We assume that the magnetic field in the EMF goes to the applied magnetic field on the outer surface of the pipe and that the induced magnetic flux density goes to zero at the inlet and outlet of the analysis domain which are far away from permanent magnets. Namely, we impose the following Dirichlet boundary condition:

$$\begin{aligned} \mathbf{b} & = 0 \quad \text{on the outer boundary surface} \\ & \text{of the analysis domain,} \end{aligned} \quad (12)$$

and therefore the surface integral does not need to be considered.

The third surface integral terms of the right-hand side of Eq. (11) on adjacent element surfaces are canceled each other, and that on the inner surface of the pipe remains. However, by using the non-slip flow condition that $\mathbf{u} = 0$, the third surface integral term vanishes on the inner surface of the pipe. The second surface integral term of the right-hand side of Eq. (11) on the outer surface of the analysis domain also vanishes since it is assumed that the pipe duct is isolated from the exterior. Namely, we impose the following boundary condition such that the normal component of the gradient of the electric field becomes zero:

$$\begin{aligned} \frac{\partial \phi}{\partial \mathbf{n}} & \quad \text{on the outer boundary surface} \\ & \text{of the analysis domain,} \end{aligned} \quad (13)$$

where \mathbf{n} is the outward normal vector on the boundary surface. Also, to determine a unique solution of the electric potential equation, it is necessary to impose

$$\phi = 0 \quad \text{on an arbitrary point inside the domain.} \quad (14)$$

When the magnetic Reynolds number Rm defined by Eq. (31) is extremely large compared to unity, an induced magnetic field freezes to flow lines and may flow out from the outlet boundary surface. In this special case, lines of magnetic force may not close on themselves in the analysis domain and therefore we should adopt the following boundary condition instead of the boundary condition (12).

$$\frac{\partial \mathbf{b}}{\partial \mathbf{n}} = 0 \quad \text{on the outlet surface.} \quad (15)$$

The two global systems of simultaneous equations described above can be solved independently, *i.e.* firstly, the induced magnetic field is determined by solving the induction equation and secondly, the electric potential equation is solved by using the induced magnetic field solution. These simultaneous equation systems have been solved by using the wave front method⁽¹²⁾.

(2) Discretization of \mathbf{A} - ϕ Formulation

In the same way as the GFEM formulation described in the previous section, the integral equations of the weighted residual of the induction equation (7) and the electric potential equation (8) are obtained as follows:

$$\begin{aligned} & \frac{1}{\mu_0} \int_V \nabla \omega \nabla A_i dV + \int_V \sigma \omega (\nabla \phi)_i dV \\ & - \int_V \sigma \omega [\mathbf{u} \times (\nabla \times \mathbf{A})]_i dV \\ & = \int_V \sigma \omega (\mathbf{u} \times \mathbf{B}_{ap})_i dV + \int_S \omega \frac{1}{\mu_0} \nabla A_i \mathbf{n} dS, \quad (16) \end{aligned}$$

$$\begin{aligned} & \int_V \sigma \nabla \omega \nabla \phi dV - \int_V \sigma \nabla \omega [\mathbf{u} \times (\nabla \times \mathbf{A})] dV \\ & = \int_V \sigma \nabla \omega (\mathbf{u} \times \mathbf{B}_{ap}) dV \\ & - \int_S \sigma \omega [\mathbf{u} \times (\nabla \times \mathbf{A})] \mathbf{n} dS \\ & - \int_S \sigma \omega (\mathbf{u} \times \mathbf{B}_{ap}) \mathbf{n} dS + \int_S \sigma \omega \nabla \phi \mathbf{n} dS. \quad (17) \end{aligned}$$

The boundary condition (12) that the induced magnetic field does not leak out leads to the expression for the boundary condition of the vector potential:

$$\mathbf{A} = 0 \quad \text{on the outer surface of the domain.} \quad (18)$$

The boundary condition which should be imposed upon the electric potential solution is Eqs. (13) and (14). The two global systems of simultaneous equations (16) and (17) have been combined and solved by using the wave front method⁽¹²⁾.

IV. FALCON Code

We have been developed a computer code, FALCON,

which permits calculation of the fine structure of the induced magnetic field and electric potential field in the EMF. The two formulations presented in the previous chapter have been implemented in the present code. In the program flow shown in Fig. 3, an applied magnetic field and a flow velocity field are required as input information of the calculation. In this chapter, we describe how to determine them.

1. Applied Magnetic Field

Any permanent magnets probably have a fabrication and arrangement tolerance and are subject to the uncertainty of a magnetization process. This generates uncertainty regarding the magnetic field which surrounds the permanent magnet and therefore the applied magnetic field should be measured after the final arrangement of the magnetic apparatus.

When such uncertainty does not need to be consider in calculations for qualitative estimation of the tendency of the EMF characteristics, it is convenient to determine the applied magnetic field with current magnetic analysis codes currently available.

2. Flow Velocity Fields

It is extremely difficult to measure three-dimensional flow velocity in a liquid metal system. We can select either of two options for treating it in the FALCON code. One is the program option to enter the result which has already been calculated with the current three-

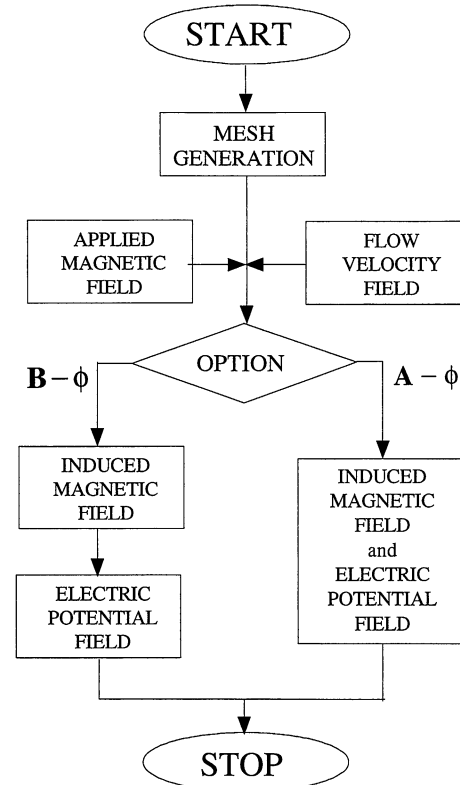


Fig. 3 Program flow of FALCON code

dimensional thermo-hydraulic analysis codes available. The other is the option to give the flow velocity distribution based on build-in models, *i.e.* an axial flow model based on the logarithmic law of a turbulent flow and a secondary flow model. In this section, we describe these build-in models.

(1) Axial Flow Model

The distribution of an axial component of a fully developed turbulent flow velocity is determined on a cross section of the pipe by assuming the logarithmic law:

$$\frac{u_z}{u^*} = 2.5 \ln(y^+) + 5.5 \quad \text{and} \quad y^+ = \frac{u^* y}{\nu}, \quad (19)$$

where u^* is the friction velocity, y is the distance from the inner surface of the pipe and ν is the kinematic viscosity of the coolant fluid. The friction velocity is determined by the averaged wall shear stress τ_w in the pipe:

$$u^* = \sqrt{\frac{\tau_w}{\rho}}, \quad (20)$$

where ρ is the fluid density. The averaged wall shear stress is determined by the following pressure balance equation:

$$\tau_w = \frac{D_h}{4} \Delta p, \quad (21)$$

where Δp is the pressure drop per unit length, and D_h is the equivalent hydraulic diameter. And the pressure drop is assumed to be expressed by

$$\Delta p = \frac{f}{2D_h} \rho \bar{u}_z^2, \quad (22)$$

where f is the friction pressure drop coefficient, and \bar{u}_z is the averaged axial flow velocity which is the input data of the FALCON code. The pressure drop coefficient in Eq. (22) is assumed to be consistent with the Blasius correlation for pipe flows:

$$f = 0.316 Re^{-0.25}. \quad (23)$$

Here, from the assumption of a fully developed flow regime, the flow velocity is independent of the coordinate z and therefore the three-dimensional flow velocity distribution can be obtained by assembling the same profile on an arbitrary cross section of the pipe.

(2) Secondary Flow Model

The bending form of the pipeline in the upstream region causes the production of a secondary flow in the pipe. To evaluate the influence of a secondary flow on the characteristics of the EMF, we have constructed two models of swirling flows based on the measured results⁽¹³⁾. One is a model of a single swirling (see Fig. 4(a)) flow which is generated by the three-dimensional bending form of the pipeline with adjacent two bends. The other is a model of a well-known double swirling (see Fig. 4(b)) flow produced in the downstream region of a single bend.

We approximate that the secondary flow on an arbitrary cross section of the pipe has the same profile. After assembling the secondary flow described below and the axial flow described in the previous section, we can ap-

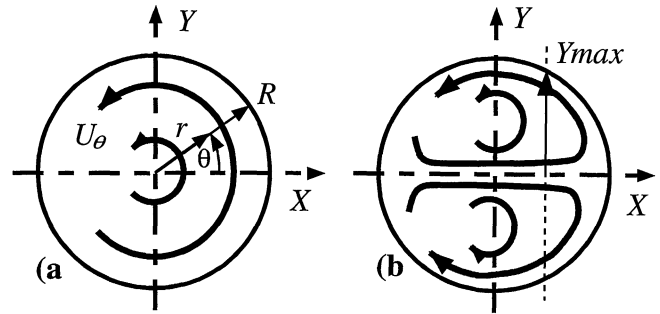


Fig. 4 Schematic of swirling flow profiles: (a) single swirling model and (b) double swirling model

proximately obtain a three-dimensional flow distribution in the pipe.

(a) Single Swirling Flow Model

According to the measured data we have approximated that a peripheral component of a flow U_θ in the cylindrical coordinate system has a linear profile and is zero at the center of the pipe:

$$U_\theta = \begin{cases} C_1 r & \text{in } 0 \leq r < R \\ 0 & \text{at } r = R \end{cases}, \quad (24)$$

where C_1 is the input parameter to determine the flow and R is the inner radius shown in Fig. 4(a). This profile can be transformed into the velocity components in the Cartesian coordinate system used in the standard formulation by using the following equations:

$$u_x = -U_\theta \sin(\theta) \quad \text{and} \quad u_y = U_\theta \cos(\theta), \quad (25)$$

where θ is the angular measure shown in Fig. 4(a).

(b) Double Swirling Flow Model

We use a new two-dimensional orthogonal coordinate system (X, Y) whose X -axis coincides with the symmetric line of the double swirling flow, as shown in Fig. 4(b), and makes an angle of θ to the x -axis of the Cartesian coordinate system used in the standard formulation. We have approximated that the X -component of the double swirling flow velocity is described as follows:

$$U_X = C_2 F(X) G(Y), \quad (26)$$

where C_2 is an input parameter to determine the flow and

$$F(X) = \left(1 - \frac{X^2}{R^2}\right), \quad G(Y) = \cos\left(\frac{\pi Y}{Y_{\max}}\right) \\ \text{and} \quad Y_{\max} = \sqrt{R^2 - X^2}. \quad (27)$$

R is the inner radius of the pipe. Because the double swirling flow must satisfy the following continuity equation:

$$\frac{\partial U_X}{\partial X} + \frac{\partial U_Y}{\partial Y} = 0, \quad (28)$$

the Y -component of the double swirling flow velocity can be determined analytically by the following integration:

$$U_Y = \int_0^Y \left(-\frac{\partial U_X}{\partial X}\right) dY$$

$$\begin{aligned}
&= \frac{2C_2XY_{\max}}{\pi R^2} \sin\left(\frac{\pi Y}{Y_{\max}}\right) \\
&\quad - \frac{2C_2X}{R^2} \left\{ Y \cos\left(\frac{\pi Y}{Y_{\max}}\right) \right. \\
&\quad \left. - \frac{Y_{\max}}{\pi} \sin\left(\frac{\pi Y}{Y_{\max}}\right) \right\}. \quad (29)
\end{aligned}$$

This profile can be transformed into a velocity field in the Cartesian coordinate system used in the standard formulation by using the following equations:

$$\begin{aligned}
u_x &= U_X \cos(\theta) + U_Y \sin(\theta), \\
u_y &= U_X \sin(\theta) - U_Y \cos(\theta). \quad (30)
\end{aligned}$$

V. Computation and Discussion

In order to check the computational efficiency and accuracy of the proposed finite element schemes based on the $\mathbf{B}\text{-}\phi$ formulation and the $\mathbf{A}\text{-}\phi$ formulation, the output voltage of the EMF instrument in the A-loop of the secondary cooling system of the Japanese Prototype Fast Breeder Reactor "MONJU" has been calculated under the calibration test conditions and compared with the result of the calibration test data⁽⁶⁾. Finally, we discuss the characteristics of the EMF in terms of a dimensionless electromagnetic expression.

1. Summary of Calibration Test

The schematic of the EMF is shown in Fig. 5. The material of the pipe is a stainless steel and its inner and outer diameter are 0.517 m and 0.557 m, respectively. The magnetic apparatus is composed of two flat permanent magnets, each of which is 1.6 m in length and 1.1 m in height. And the EMF has 7 pairs of electrodes which are welded to the center position and the right half region of the pipe within the magnetic circuit. The 6 pairs of electrodes are assembled at right angles with flat-to-flat direction of the magnets. The electrode No. 7 is inclined at a 30-degree angle with the other electrodes. The fluid used is a liquid sodium.

The x -component of the applied magnetic field was measured along the center line of the pipe as shown in Fig. 6. The magnitude of the magnetic field at the center of the magnetic circuit was about 0.023 T. The value on the outside of the measured range and the y - and z -components of the applied magnetic field have been assumed to be negligible. The flow conditions were 100/60/20% of the full-power operation condition of the MONJU reactor and the averaged flow velocities were 5.68/3.33/1.11 m/s, respectively. The temperature conditions were 200/285/325°C. The range of the magnetic Reynolds number Rm was 3.9 to 27.6. Here, the magnetic Reynolds number Rm is the ratio of convection and diffusion of a magnetic field and is defined as follows:

$$Rm = \mu_o \sigma \bar{u}_z D_h, \quad (31)$$

where D_h is the hydraulic diameter and \bar{u}_z is the averaged flow velocity. If Rm is large compared to unity, the relative importance of convection becomes large.

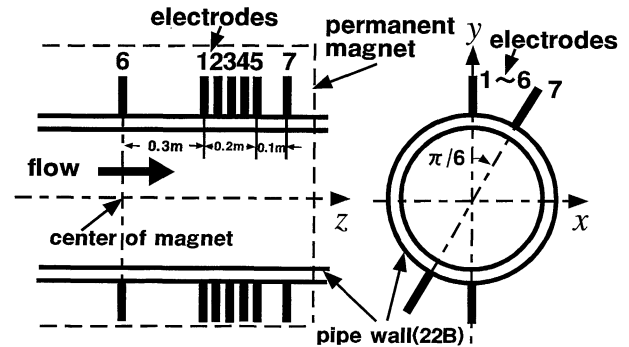


Fig. 5 Schematic of EMF in secondary cooling loop of MONJU

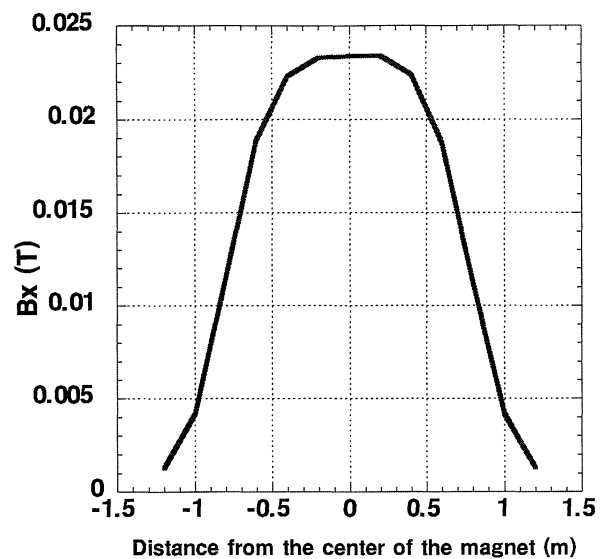


Fig. 6 Axial distribution of the applied magnetic field

2. Computational Efficiency

In this section, we have compared the computational efficiency and the accuracy of results between the $\mathbf{B}\text{-}\phi$ formulation and the $\mathbf{A}\text{-}\phi$ formulation based on the Coulomb gauge. We have calculated the output voltage of the EMF under the condition of the magnetic Reynolds number $Rm = 27.6$ where the effect of the induced magnetic field is the largest within this test range.

We adopted the mesh scheme on the cross-section of the pipe shown in Fig. 2. The whole analysis domain is divided into three regions in the axial direction. The axial length and mesh size is 2.5 m and 0.15625 m in the upstream region, 1.6 m and 0.05 m in the middle region where the magnets are positioned, and 3.5 m and 0.0875 m in the downstream region. The center of the magnets is positioned at the center of the middle region. The total number of axial meshes is 88. In the whole analysis domain, the number of finite elements is 4,928 and the number of nodes is 41,385. In the $\mathbf{B}\text{-}\phi$ formulation, the number of unknown variables is 124,155 for the magnetic field solution and 41,385 for the electric potential solution. And in the $\mathbf{A}\text{-}\phi$ formulation, the number

of unknown variables was 165,540 for the simultaneous solution of the vector potential and the electric potential. This mesh scheme has been selected suitably by checking the asymptotic trend of the solution in the mesh size. Also, considering that the induced magnetic field is transported by the liquid metal fluid flow, we have made the axial length in the downstream region longer. The length of the analysis region is determined by searching axial positions where predicted output voltage can be approximated to go to zero.

Figure 7 shows the axial distributions of the predicted electric potential differences between top and bottom points on the outer surface of the pipe, *i.e.* between electrodes assembled at right angles with flat-to-flat direction of the magnets. The calculation results show that the output voltages predicted by the $B\text{-}\phi$ formulation and the $A\text{-}\phi$ formulation agree closely and that the computational accuracy of the two formulations is almost equal within the present condition of the high magnetic Reynolds number. Also, the CPU time on computer system with Alpha chip (600 MHz) was 11,940s with the $B\text{-}\phi$ formulation and 28,320s with the $A\text{-}\phi$ formulation. In the present mesh scheme, the calculation with the $B\text{-}\phi$ formulation is over two times faster than that with the $A\text{-}\phi$ formulation based on the Coulomb gauge in which the governing equations (7) and (8) must be solved simultaneously, and therefore we select the $B\text{-}\phi$ formulation for the calculation described in the next section.

3. Simulation of Calibration Test

We have simulated the calibration test of the EMF by using the $B\text{-}\phi$ formulation and have compared the predicted output voltages with the calibration test results. The mesh scheme described in the previous section has been used in the present calculation. According to the test condition, the turbulent flow profile of the axial flow

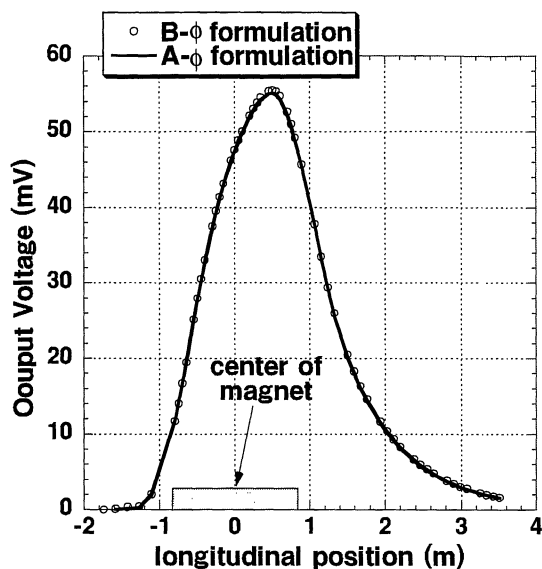


Fig. 7 Comparison between results by $A\text{-}\phi$ and $B\text{-}\phi$ formulations

velocity component has been approximately determined by using the logarithmic law and adjusted by the mean flow velocity measured. Also, the swirling flow component has been assumed not to exist.

Figure 8 shows the predicted output voltages V_{cal} of all electrodes compared with the measured data V_{exp} . The relative difference between the predicted and measured results $\Delta V_{rel} = (V_{cal} - V_{exp})/V_{exp}$ is -5.0 to 0.4% within the range of the calibration test condition, as shown in Table 1. The predicted results of the greater part of the electrodes, *i.e.* Nos. 1 to 5 which are ordinarily used for monitoring, agree well with measured results within the relative difference of -1.8 to 0.4% . In the electrode No. 6 at the center of the magnet, the values of ΔV_{rel} are large at the highest Rm case within each temperature condition and the largest value is -3.5% . In the inclined electrode No. 7 near the outlet side of the magnet, the values of ΔV_{rel} are larger than those in the other electrodes and become large at the lowest Rm case within each temperature condition. The largest value is -5.0% . We will discuss the cause of these prediction error below.

Considering the fact that the output voltages of the electrode Nos. 1 to 5 are predicted well, we cannot explain the cause of the large relative differences of the electrode Nos. 6 and 7 by the prediction error of induced magnetic fields and the uncertainty of the flow profile used. The uncertainty of the three-dimensional profile of the applied magnetic field used seems to be the most probable for explaining the cause. In the present calculations, we have assumed that the applied magnetic field on any cross-section of the pipe has the same profile. The profile on the cross-section at the end of the magnet is indeed different from that within the magnet region. Assuming the uncertainty of the applied magnetic field at

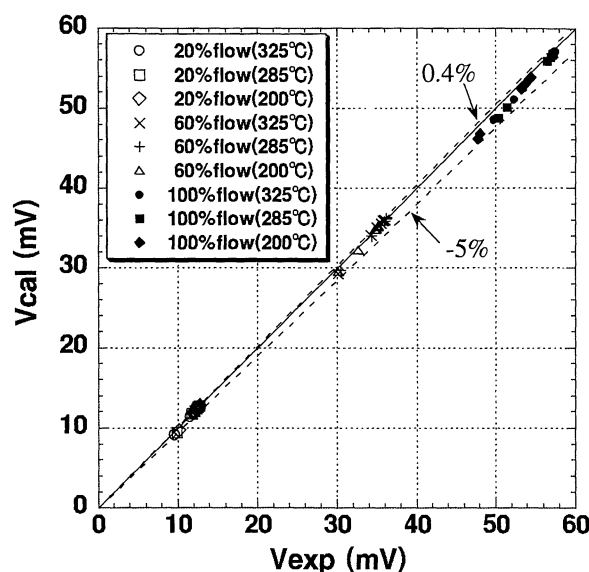


Fig. 8 Comparison between the predicted and measured output voltage of the EMF in MONJU secondary cooling system

Table 1 Relative difference between predicted and measured output voltage

Rm	$\Delta V_{rel} = (V_{cal} - V_{exp})/V_{exp}$ at electrode Nos. 1 to 7						
	No. 1	No. 2	No. 3	No. 4	No. 5	No. 6	No. 7
Coolant temperature: 325°C							
3.9	-0.2%	-0.3%	-0.7%	-1.1%	-1.1%	-0.6%	-4.0%
11.6	0.2%	0.4%	0.4%	0.1%	0.2%	-0.5%	-2.8%
19.7	-1.0%	-0.9%	-0.6%	-0.7%	-0.8%	-2.5%	-2.4%
Coolant temperature: 285°C							
4.3	0.0%	0.1%	-0.5%	-0.9%	-0.8%	-0.5%	-4.9%
12.8	0.1%	0.2%	0.1%	0.0%	-0.3%	-0.9%	-2.3%
22.0	-1.2%	-1.0%	-0.8%	-0.8%	-0.9%	-2.7%	-3.4%
Coolant temperature: 200°C							
5.4	-0.3%	-0.4%	-0.7%	-1.1%	-1.4%	-1.1%	-5.0%
16.0	-0.1%	0.2%	0.3%	0.1%	0.1%	-1.4%	-2.4%
27.6	-1.8%	-1.4%	-1.4%	-1.2%	-1.1%	-3.5%	-2.7%

both ends of the magnet and considering the end effect due to the induced magnetic field described in the next section, we can infer that:

- (1) the output voltage of the electrode No. 6 is controlled by the summation of the applied magnetic field within the magnet region and the induced magnetic field produced by the applied magnetic field at the upstream end of the magnet, and therefore by the convection of this induced magnetic field, the relative difference of the electrode No. 6 in the highest Rm case becomes large, and
- (2) because the electrode No. 7 is near the downstream end of the magnet, the output voltage is mainly controlled by the applied magnetic field near the magnet end and the induced magnetic field produced by the applied magnetic field at the magnet end. The relative differences become larger than those in the other electrodes by the uncertainty of the applied magnetic field, and also those become large at the lowest Rm case because the effect of the induced magnetic field reduces as Rm increases by the convection effect.

Consequently, the present study has indicated the possibility that computer simulation can be used to predict the characteristics of the EMF in a liquid metal system and that the accurate information of the profile of the applied magnetic field is necessary for predicting them quantitatively.

4. Effect of Induced Magnetic Field

A special feature of the EMF for a liquid metal flow measurement is the fact that the output voltage is strongly influenced by the induced magnetic field. In order to study qualitatively the effect of the induced magnetic field on the characteristics of the EMF, we utilize the following dimensionless electromagnetic expression.

The following dimensionless quantities are defined:

$$\begin{aligned}\hat{\mathbf{b}} &= \mathbf{b}/B_o, \quad \hat{\phi} = \phi/(\bar{u}_z B_o D_h), \quad \hat{\mathbf{B}}_{ap} = \mathbf{B}_{ap}/B_o, \\ \hat{\mathbf{x}} &= \mathbf{x}/D_h, \quad \hat{\mathbf{u}} = \mathbf{u}/\bar{u}_z.\end{aligned}\quad (32)$$

The induction equation (5) and the electric potential equation (2) are rearranged by using Eqs. (31) and (32), as follows:

$$\begin{aligned}\frac{1}{Rm} \nabla^2 \hat{\mathbf{b}} + [(\hat{\mathbf{b}} \nabla) \hat{\mathbf{u}} - (\hat{\mathbf{u}} \nabla) \hat{\mathbf{b}}] \\ + [(\hat{\mathbf{B}}_{ap} \nabla) \hat{\mathbf{u}} - (\hat{\mathbf{u}} \nabla) \hat{\mathbf{B}}_{ap}] = 0,\end{aligned}\quad (33)$$

$$\nabla^2 \hat{\phi} - \nabla[\hat{\mathbf{u}} \times (\hat{\mathbf{b}} + \hat{\mathbf{B}}_{ap})] = 0,\quad (34)$$

where B_o is the applied magnetic flux density at the center of a magnetic circuit. Here, it should be noted that the electromagnetic phenomenon of EMFs is controlled by the magnetic Reynolds number Rm . A dimensionless output voltage \hat{V} is defined by a electric potential difference V between a pair of electrodes, as follows:

$$\hat{V} = V/\bar{u}_z B_o D_h.\quad (35)$$

Rearranging Eq. (35) by using Eq. (31), the following relationship is obtained:

$$\hat{V} = \left(\frac{\mu_o \sigma}{B_o} \right) \frac{V}{Rm} \propto \frac{V}{Rm}.\quad (36)$$

Namely, a dimensionless output voltage is related to a gradient of the output voltage with respect to Rm .

In the EMF of the present study, the position of the electrodes is symmetric around the axis of the pipe. For the simplification of the discussion, it is assumed that the flow velocity distribution is axisymmetric. This assumption is a fairly good approximation when the flow is fully developed.

When the value of Rm is extremely small compared to unity, the induced magnetic field can be neglected with respect to the applied magnetic field. The dimensionless output voltage does not change, if the averaged flow ve-

locity changes under the condition of $Rm \ll 1$. Namely, it is noted that if the induced magnetic field can be neglected, the dimensionless output voltage of EMF is held uniform and the output voltage is determined only by the applied magnetic field, *i.e.* it is proportional to the average flow velocity. Let us express this output voltage by V_{ap} .

Conversely, when the value of Rm is extremely large compared to unity, *i.e.* the convection of the induced magnetic field is larger than the diffusion of it, the flow has a large influence on the magnetic field in the EMF. Therefore, the dimensionless output voltage of EMF is not held uniform and the output voltage is not in proportion to the average flow velocity. In Fig. 1, the primary direction of the induced magnetic field produced by the induced current J_3 in the inlet region of the magnet is opposite to that of the applied magnetic field. However, the primary directions of the applied magnetic field and the induced magnetic field produced by the induced current J_4 in the outlet region is the same. Namely, within the extent of the induced magnetic field in the inlet region, the output voltage V becomes small compared to V_{ap} . And, within the extent of the induced magnetic field in the outlet region, the output voltage V becomes large compared to V_{ap} . The difference $V_{in} (= V - V_{ap})$ represents a change of the output voltage due to these induced magnetic fields. In the inlet region, V_{in} is negative and in the output region, V_{in} is positive. This effect is called the end effect. The extent of the end effect spreads toward the downstream direction by the convection of the induced magnetic field. In a liquid metal system, this effect is an important factor controlling the performance of an EMF.

From the rationale described above, the following normalized dimensionless output voltage will be useful as a way of directly representing the effect of the induced magnetic field on the output voltage:

$$\hat{V}/\hat{V}_{ap} = 1 + \hat{V}_{in}/\hat{V}_{ap}. \tag{37}$$

In the present study, using the dimensionless output voltage at the minimum Rm value \hat{V}_{min} which has been already obtained, we adopt another normalized expression \hat{V}/\hat{V}_{min} similar to \hat{V}/\hat{V}_{ap} . A value of \hat{V}/\hat{V}_{min} represents the ratio of the gradients expressed by Eq. (36) at a certain Rm value and at the minimum Rm value. If \hat{V}/\hat{V}_{min} increases or decreases compared to unity as Rm increases, a gradient becomes more or less steep compared to the gradient at the minimum Rm value. It is noted that the expression \hat{V}/\hat{V}_{min} represents relatively the effect of the induced magnetic field on the output voltage. **Figure 9** shows the normalized dimensionless output voltage \hat{V}/\hat{V}_{min} as a function of Rm , using the measured and predicted results.

We investigate how far the influence of the induced magnetic field extends. Figure 9 shows that \hat{V}/\hat{V}_{min} of electrode No. 6 decreases monotonously, and that those of electrode Nos. 1 to 5 and 7 within the right-half region of the magnet increase at $Rm = 3.9$. Considering that

these tendency is mainly determined by the relative importance of each of the positive and negative end effects, we can infer that the positive end effect extends from the magnet outlet end to the position of No. 1 electrode, *i.e.* 0.3 m from the center of the magnet, at $Rm = 3.9$. Also, it is observed in Fig. 9 that of electrode Nos. 1 to 5 and 7 decrease as Rm increases over a certain value of Rm , and that the values of \hat{V}/\hat{V}_{min} of all electrodes are less than unity at $Rm = 27.6$. From this fact, we can infer that the negative end effect produced in the inlet region of the magnet extends within the right-half region of the magnet at $Rm = 27.6$.

Next, we investigate the characteristics of the voltage response with respect to Rm . From the rationale described above it is noted that as a value of \hat{V}/\hat{V}_{min} becomes less than unity, the gradient of the voltage response curve becomes less steep than that at $Rm = 3.9$, *i.e.* a sensitivity of the EMF output becomes worse. It is observed in Fig. 9 that \hat{V}/\hat{V}_{min} at all electrodes becomes

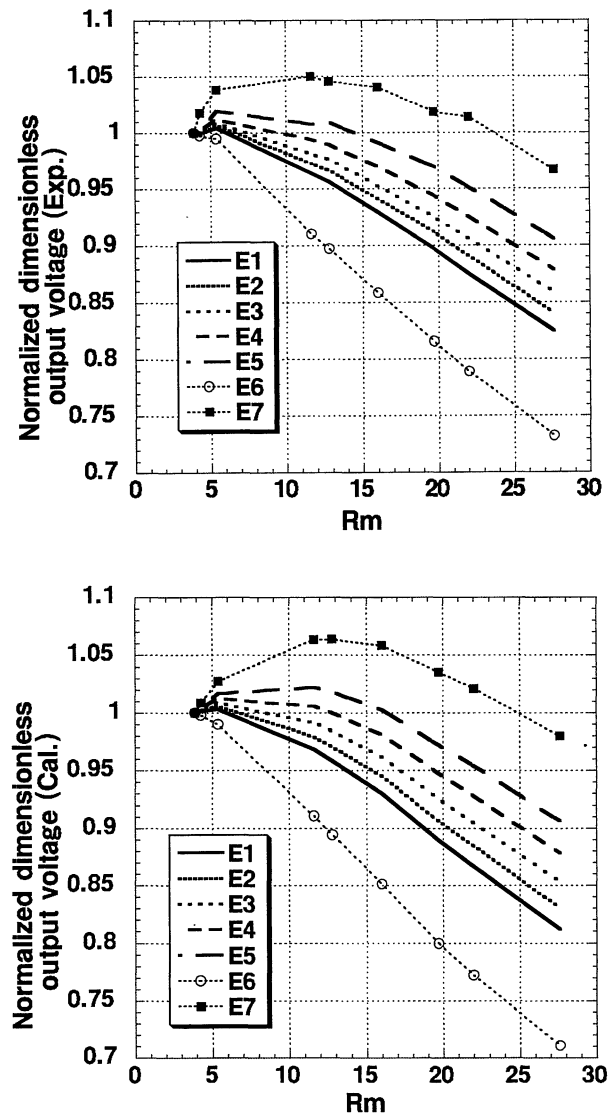


Fig. 9 Normalized dimensionless output voltage of secondary loop EMF's electrodes

less than unity, and that a deviation from unity is the least at electrode No. 7. This indicates that the voltage response of electrode No. 7 has the best sensitivity.

From the results of the present study, it should be noted that we can anticipate the improvement of the output voltage and linearity of the EMF response by utilizing the end effect. Also, the results indicates the possibility that an EMF with excellent performance can be designed through the optimization of electrode position by using computer simulation.

VI. Conclusion

A numerical technique to predict the three-dimensional steady-state structure of electromagnetic phenomena in the Faraday-type Electromagnetic Flow Meter (EMF) has been adopted and formatted as a computer code, FALCON. The numerical solution method based on the B - ϕ formulation works efficiently and accurately.

The computer simulation of the calibration test of the EMF in the MONJU secondary cooling system has been performed and the calculations have shown a good agreement with the experiments. This study has demonstrated that computer simulation can be used to investigate complicated induced magnetic phenomena which current experimental techniques cannot fully acquire.

We have proposed dimensionless expressions for estimating the effect of the induced magnetic field. The present dimensionless analysis has indicated the possibility that the EMF performance can be improved through the investigation of the induced magnetic field and the optimization of electrode position.

Overall, this study has indicated that the present simulation method can be applied to the estimation of the characteristics of an EMF and the design of a new EMF.

[NOMENCLATURE]

B_{ap} :	Applied magnetic field (T)
b :	Induced magnetic field (T)
D_h :	Equivalent hydraulic diameter (m)
f :	Friction pressure drop coefficient
J :	Induced electric current (A)
n :	Outward normal vector
R :	Inner radius of pipe (m)
u :	Flow velocity (m/s)
u^* :	Friction velocity (m/s)
U_θ :	Peripheral flow velocity (m/s)
V :	Output voltage of EMF (V)
y :	Distance from the inner surface of pipe (m)
Δp :	Pressure drop per unit length (Pa)
μ_0 :	Magnetic permeability of vacuum ($4\pi \cdot 10^{-7}$ H/m)
ν :	Kinematic viscosity (m^2/s)
ξ :	Curvilinear coordinate
ρ :	Fluid density (kg/m^3)
σ :	Electric conductivity (S/m)
τ_w :	Averaged wall shear stress (N/m)

ϕ : Electric potential (V)

(Subscript)

ap : Applied magnetic field

cal : Computation result

exp : Measured result

i : Component of Cartesian coordinate

(Superscript)

$\bar{\quad}$: Averaged value

$\hat{\quad}$: Dimensionless quantity

ACKNOWLEDGMENT

The authors are grateful thanks to Japan Nuclear Cycle Development Institute (JNC) for opening the calibration test data for the Faraday-type Electromagnetic Flowmeter in the secondary cooling system of the Japanese Prototype Fast Breeder Reactor, "MONJU" to the public.

—REFERENCES—

- (1) Shercliff, J. A.: "The Theory of Electromagnetic Flow-Measurement", the University Press, Cambridge, United Kingdom, (1962).
- (2) Bevir, M. K.: *J. Fluid Mech.*, **43**, 577 (1970).
- (3) Kuromori, K.: *Trans. SICE*, 29[12], 1413 (1993), [in Japanese].
- (4) Kobayashi, S., Kudou, A.: *Nihon-Genshiryoku-Gakkai Shi, (J. At. Energy Soc. Jpn.)*, 11[11], 7 (1969), [in Japanese].
- (5) Shimizu, T., *et al.*: *Trans. JCME (C)*, **60**, 576 (1994), [in Japanese].
- (6) Sakaba, H., *et al.*: *PNC ZN 9410*, 91-354 (1989), [in Japanese].
- (7) Finlayson, B. A.: "The Method of Weighted Residuals and Variational Principles", Academic Press, New York, 226 (1972).
- (8) Zienkiewicz, O. C.: "The Finite Element Method", (3rd ed.), McGraw-Hill, (1977).
- (9) Thompson, J. F., Thames, F. C., Mastin, C. W.: *NACA-CR-2729*, 628-631 (1978).
- (10) Shimizu, T., Ninokata, H., Shishido, H.: *Nucl. Eng. Des.*, **120**, 369-383 (1990).
- (11) Zienkiewicz, O. C., Heinrich, J. C.: "Finite Element in Fluids", John Wiley & Sons, Vol. 3, p. 1-22 (1978).
- (12) Shimizu, T.: *Trans. JCME (B)*, **63**, 798 (1997), [in Japanese].
- (13) Murakami, M., *et al.*: *Trans. JCME(2)*, **35**, 272 (1969), [in Japanese].

[APPENDIX]

1. Mathematical Formulas

$$\nabla \times (\nabla \times \mathbf{b}) = -\nabla^2 \mathbf{b} + \nabla(\nabla \cdot \mathbf{b})$$

in Cartesian coordinate system (A1)

$$\nabla \times (\mathbf{u} \times \mathbf{b}) = (\mathbf{b} \cdot \nabla) \mathbf{u} - (\mathbf{u} \cdot \nabla) \mathbf{b} + \mathbf{u}(\nabla \cdot \mathbf{b}) - \mathbf{b}(\nabla \cdot \mathbf{u}) \quad (\text{A2})$$